

Temperature Distribution and Heat Transfer in Narrow Channel during Thermoacoustic Oscillation

TADASHI WATANABE

Research Institute of Nuclear Engineering,
University of Fukui,
Kanawa-cho 1-3-33, Tsuruga-shi, Fukui-ken 914-0055,
JAPAN

Abstract: - Thermoacoustic oscillation is induced when a gas is in a tube with a narrow channel section that has a large temperature gradient. Although the oscillation in the tube section was studied, that in the narrow channel has not yet been discussed well. The temperature distribution and the heat transfer in the narrow channel section, which are the most important parameters for the design of thermoacoustic devices, are discussed in this study. Numerical calculations of fluid conservation equations are performed, and the onset of oscillation is obtained by gradually increasing the temperature gradient. The minimum onset temperature ratio is shown to agree with the existing analytical and experimental results. The average wave speed is in between the isothermal sound speed for the highest temperature and the adiabatic sound speed for the lowest temperature. The distribution of oscillating temperature in the narrow channel is found to be different and reversed from that in the tube. It is shown in the narrow channel that the heat transfer is smaller for larger diameter and larger for smaller diameter and the heat transfer coefficient or the heat transfer model should be improved for the oscillating flow.

Key-Words: - Thermoacoustic oscillation, Onset temperature ratio, Temperature distribution, Heat transfer, Narrow channel

Received: June 9, 2022. Revised: March 19, 2023. Accepted: May 15, 2022. Published: June 29, 2023.

1 Introduction

When a gas is in a tube with a narrow channel section that has a large temperature gradient, spontaneous gas oscillation known as thermoacoustic oscillation is induced, [1]. The thermoacoustic oscillation is caused by the irreversible heat exchange between the gas and the channel wall, [2], and the thermal energy is converted to the kinetic energy of gas oscillation. Experimental and analytical studies were performed, and the early-stage results were reviewed, [3], [4], [5], [6]. Since the temperature gradient or difference alone is needed for thermoacoustic devices, the pressure and temperature conditions, gas type, tube design, and so on have been studied thereafter experimentally, [7], [8], [9], [10], [11], [12], [13], and analytically, [12], [14], [15], [16], [17], [18], [19], [20], [21]. The applications for thermoacoustic refrigerators, [22], and electric power generation, [23], were reviewed as typical examples. The practical applications for power generation were proposed such as electric generators for rural communities, [24], [25], a generator utilizing low-grade heat sources, [26], and a reliable low-cost system, [27]. The thermoacoustic temperature

sensor was proposed in the nuclear engineering field to monitor the neutron flux and fuel condition, [28], [29]. The applications were of primary interest and the oscillation in the tube section was mainly discussed in these studies. The oscillation of variables in the narrow channel section, however, has not yet been studied well.

The analytical treatments of thermoacoustic oscillation are almost based on the linearized equations representing the oscillation of pressure and velocity around the mean values with the assumption of temperature distribution, [30]. Fluid conservation equations were not solved but the stability limit was estimated using this acoustic approximation, [31]. Two-dimensional flow fields around the narrow channel were discussed using computational fluid dynamics codes such as CFX, [32], [33], and Fluent, [34], [35], [36]. Although fluid equations were solved directly and velocity and temperature distributions were shown, the computational region was limited and several assumptions were needed for boundary and initial conditions. It was shown by the numerical simulation that the thermoacoustic oscillation was induced using one-dimensional fluid conservation

equations, [37]. The heat transfer coefficient was, however, assumed to be a constant and suddenly increased for the onset of oscillation, and the time variations of oscillating variables alone were shown.

The thermoacoustic oscillation does not need electricity, and the application is desirable in the nuclear engineering field during station blackout accidents, [28], [29]. The mechanism of oscillation in the narrow channel section is, however, not yet clearly understood. In this study, the time variations and spatial distributions of temperature, velocity, and pressure in the thermoacoustic loop, especially in the narrow channel section, are made clear. Numerical simulations are performed by solving the compressible mass, momentum, and energy conservation equations for a working fluid to include nonlinear effects. The heat conduction equations for wall structures of whole the thermoacoustic loop are solved simultaneously. According to the experimental procedure in [31], realistic initial and boundary conditions are applied. The dependence of simulated results on the number of calculation cells is checked, and quantitative results are obtained. The heat transfer in the narrow channel section, which is one of the most important parameters for the design of a thermoacoustic loop, is discussed.

2 Simulation Method

2.1 Governing Equations

The gas flow is simulated by solving one-dimensional compressible conservation equations. The mass conservation equation is given by

$$A \frac{\partial \rho}{\partial t} + \frac{\partial \rho u A}{\partial x} = 0, \quad (1)$$

where A , ρ and u are the flow area, density, and velocity, respectively. The momentum conservation equation is given by

$$\rho A \frac{\partial u}{\partial t} + \frac{1}{2} \rho A \frac{\partial u^2}{\partial x} = -A \frac{\partial p}{\partial x} + \rho g A - f_w, \quad (2)$$

where p , g , and f_w are the pressure, gravitational acceleration, and wall friction, respectively. The wall friction is defined by

$$f_w = \lambda \frac{\rho u^2}{2} p_e, \quad (3)$$

where λ and p_e are the friction factor and the perimeter, respectively. The friction factor is given according to the Reynolds number, Re , by

$$\lambda = \frac{64}{Re}, \quad 0 \leq Re \leq 2200 \quad (4)$$

$$\frac{1}{\sqrt{\lambda}} = -2 \log \left\{ \frac{\varepsilon}{3.7D} + \frac{2.51}{Re} \left[1.14 - 2 \log \left(\frac{\varepsilon}{D} + \frac{21.25}{Re^{0.9}} \right) \right] \right\}, \quad 3000 \leq Re \quad (5)$$

where D is the diameter of a narrow channel or tube and ε is the surface roughness. The Reynolds number is defined by $Re = (\rho u D / \mu)$, where μ is the viscosity. The friction factor between the laminar and turbulent flows is calculated by interpolation. The energy conservation equation is given by

$$A \frac{\partial \rho U}{\partial t} + \frac{\partial \rho u U A}{\partial x} = -p \frac{\partial u A}{\partial x} + q_w, \quad (6)$$

where U and q_w are the internal energy and wall heat transfer, respectively. The wall heat transfer is defined by

$$q_w = h_w p_e (T_w - T_g), \quad (7)$$

where h_w is the heat transfer coefficient, and T_w and T_g are the wall and gas temperatures, respectively. The heat transfer coefficient is given as the Nusselt number,

$$Nu = 4.36, \quad 0 \leq Re \leq 2200 \quad (8)$$

$$Nu = 0.023 Re^{0.8} Pr^{0.4}, \quad 3000 \leq Re \quad (9)$$

where Nu and Pr are the Nusselt and Prandtl numbers, respectively defined by $Nu = (h_w D / k)$ and $Pr = (\mu C_p / k)$, where k and C_p are the thermal conductivity and specific heat, respectively. The Nusselt number between the laminar and turbulent flows is obtained by interpolation.

Tube and channel walls are assumed to be annular, and a one-dimensional heat conduction equation in the radial direction is given by

$$(\rho C_p)_w \frac{\partial T}{\partial t} = \frac{1}{r} \left[\frac{\partial}{\partial r} \left(r k_w \frac{\partial T}{\partial r} \right) \right], \quad (10)$$

where $(\rho C_p)_w$, T , and k_w , respectively, are the volumetric heat capacity, temperature, and thermal conductivity of the wall.

The governing equations are calculated using the RELAP5 code as a numerical solver, which is designed to simulate the fluid flow and the structural temperature in nuclear reactors, [38].

2.2 Numerical Model

The numerical model is based on the closed-loop device used in the experiment, [31], and in the simulation, [37], and is briefly described here. The outline of the numerical model is shown in Figure 1. The closed loop is 2.8 m in length and consists of four straight tubes with a length of 0.7 m, an inner diameter of 40 mm, and a wall thickness of 1.2 mm. A short section of the left tube in Figure 1 is replaced by a bundle of narrow channels called a stack. The stack length is 35 mm, and the diameter of the narrow channel is from 0.2 mm to 2.0 mm. The porosity of the stack, which is the ratio of the flow area between the tube and all of the narrow channels, is 0.67. One side of the stack is kept at a high temperature by the hot heat exchanger, HX, and the other side is kept at a low temperature by the cold HX. The length of the hot and cold HXs is 13 mm. The flow area of HX is 0.67 of the tube flow area. The working fluid is air, and the tube and HXs are made from stainless steel while the stack is made from ceramic.

The initial temperature is 295 K for the gas, walls, and outside of the tube. The outer surface temperature of hot HX, T_h , is set at a higher value at time zero, while that of cold HX, T_c , is unchanged. The temperature gradient along the outer surface of the stack is linear between the hot and cold HXs. The heat transfer coefficient is 5 W/(m²K) for the outer surface of the tube. After the steady-state flow field is established, T_h is increased by 5 K. The temperature gradient along the stack is modified simultaneously. If the oscillating flow is observed, this T_h is regarded as the onset temperature. If the oscillation is not calculated, the steady-state calculation is performed again with 5 K higher T_h . These boundary conditions and procedures were applied for simulating the experimental procedure [31].

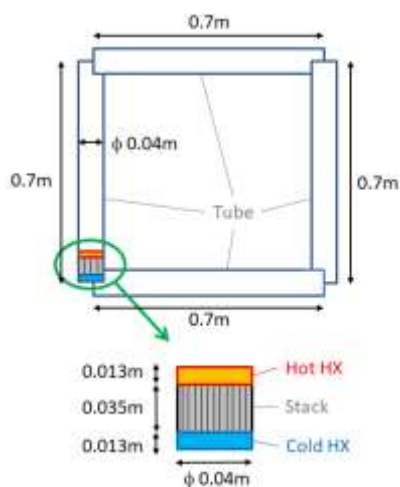


Fig. 1: Outline of numerical model

3 Results and Discussion

3.1 Dependence on Calculation Cells

The dependence of simulated results on the number of calculation cells, which is not always checked in numerical approaches, [32], [34], [37], is shown here for quantitative discussion. A typical example is shown in Figure 2, where the relative values of steady-state velocity and pressure are depicted. The steady-state flow field is established up to 3000 s of calculation, and the results at 5000 s are shown in Figure 2. It is seen that the calculated results using a smaller number of cells are smaller than those using a larger number of cells and the effect is notable for the number of cells smaller than 200.

The number of calculation cells in this study is, thus, determined to be 281, since the calculated results are not affected when the number of cells is larger than 250. Each fluid cell has a six-mesh wall structure, in which the heat conduction is calculated using the material properties of the walls. The effect of calculation cells in the wall is found to be negligibly small, and not shown here. The time step size used for the steady-state calculation is ranging from 0.1 ms to 1.0 ms according to the diameter of the narrow channel to obtain undisturbed flow fields, and the time step size after the steady state is 0.015 ms in the following simulations. These values of time step size are determined so that the Courant number based on the cell size and the sound speed becomes less than unity.

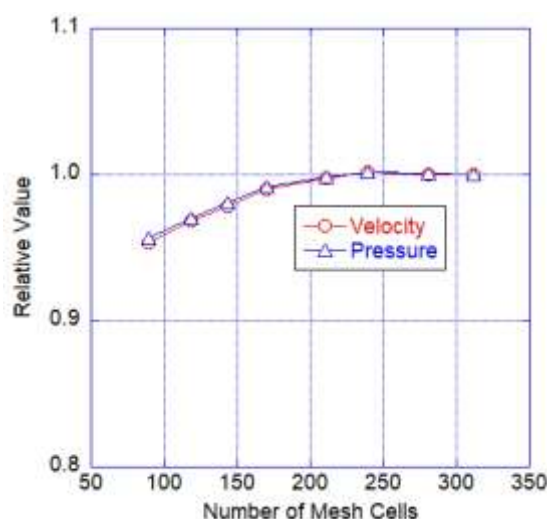


Fig. 2: Dependence of flow field on calculation cells

3.2 Onset of Thermoacoustic Oscillation

The variations of gas temperatures at four locations in the loop are shown in Figure 3 after the steady state. The diameter of the narrow channel is 0.8 mm,

and the surface roughness is zero in this case. The selected locations are the stack mid-elevation, $(1/4)L$, $(2/4)L$, and $(3/4)L$, where L is the loop length and $(1/4)L$, $(2/4)L$ and $(3/4)L$ are the distances along the loop from the cold HX. The four locations are almost corresponding to the four corners in Figure 1. Two cases with different T_h , 435 K and 440 K, are indicated in Figure 3 after the steady state.

The steady-state temperature at 5000 s is higher in the stack and decreases along the tube since the outside temperature is the same as the initial temperature of 295 K and the heat transfer between the outer surface of the tube and the environment is calculated. The outer surface is thus cooled by the environment, and the gas temperature decreases along the tube.

The maximum Reynolds number, Re , is about 7.9 and 271.1, respectively, in the stack and the tube due to a small circulating flow. The steady-state flow is, thus, laminar, and the laminar friction factor, Eq. (4), and heat transfer coefficient, Eq. (8), are used up to 5000 s. It is noted that the steady state was established much earlier when the heat transfer coefficient was fixed at a small value, [37], while the heat transfer coefficient is given theoretically and varied according to the gas temperature in this study. The heat transfer rate is thus affected by the circulating flow and the wall temperature, and a longer time is needed to obtain a steady state.

The thermoacoustic oscillation is shown to occur at about 5008 s for the case with T_h of 440 K in Figure 3. It is also shown that the oscillation is not induced when T_h is 435 K. After the onset of oscillation, the oscillation amplitude is larger in the stack than at the other locations of the tube. This is because the thermal energy is input to the gas in the stack, and the oscillation energy is the maximum in the stack.

The temperatures at $(1/4)L$, $(2/4)L$, and $(3/4)L$ decrease slightly and oscillate. The decrease in temperature indicates a cooling effect since the oscillating velocity is much larger than the steady-state circulating velocity. The maximum Re is about 64.3 and 6307, respectively, in the stack and the tube during the oscillation. The laminar friction factor and the heat transfer coefficient are used in the stack while the laminar and turbulent correlations are used in the tube after the onset of oscillation. The heat transfer coefficient is larger for the turbulent flow, and the cooling effect becomes larger during the oscillation in the tube.

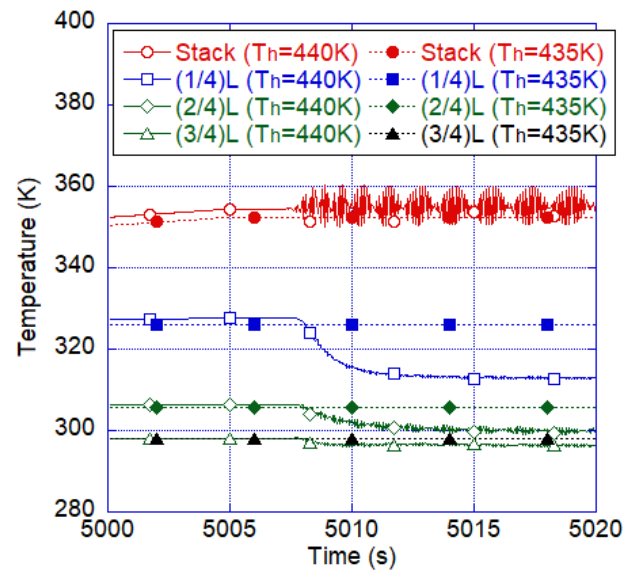


Fig. 3: Variations of gas temperatures at four locations after the steady state.

3.3 Temperature Distribution and Wave Speed

The temperature distributions along the loop at 5000 s and 5020 s are shown in Figure 4(a), where the location is the distance from the cold HX along the loop normalized by the loop length. The gas temperature increases steeply in the stack from the cold HX at the location of 0.0 to the hot HX at about 0.022 and decreases gradually in the loop from the hot to cold HXs.

The temperature distribution at 5020 s is lower than that at 5000 s in the tube section. This shows the cooling effect of oscillation as shown in Figure 3. The heat transfer rate is larger for the oscillating flow at 5020 s due to the turbulent heat transfer coefficient. The temperature distribution thus becomes lower than the steady-state distribution as shown in Figure 4(a). The heat transfer rate depends also on the temperature difference between the gas and the wall. The gas temperature becomes lower downstream, where the location becomes larger than about 0.5. The heat transfer rate is, thus, smaller in the downstream, and the cooling effect due to the turbulent heat transfer is not notable in the downstream.

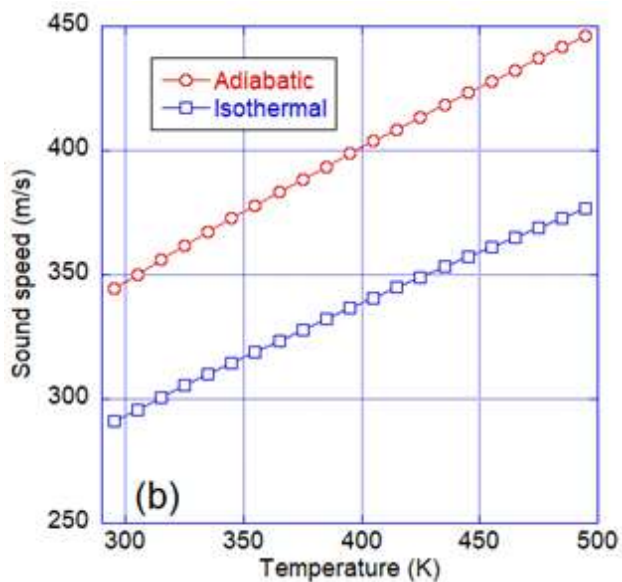
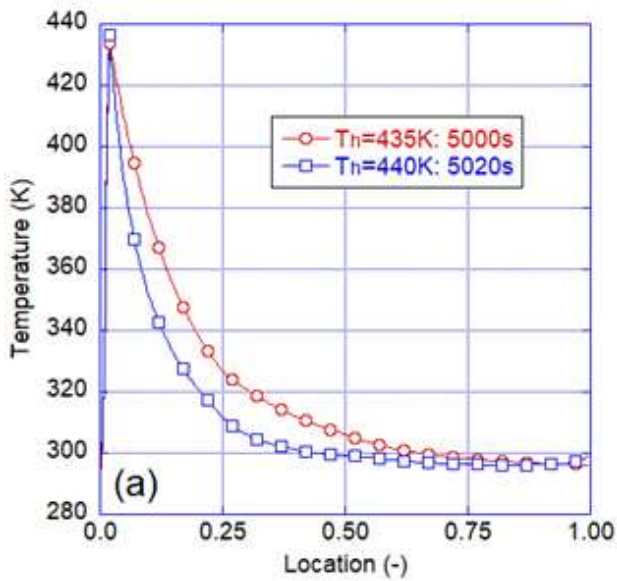


Fig. 4: Temperature distributions along the loop (a) and relation between the sound speed and the temperature (b).

The relation between the sound speed and the temperature of air under atmospheric pressure is shown in Figure 4(b). The oscillation frequency is 125.8 Hz in Figure 3, and the average wave speed along the loop is estimated to be 352.2 m/s. Under the adiabatic condition, the temperature corresponding to this sound speed is 308.3 K, while 432.5 K is under the isothermal condition as shown in Figure 4(b). These temperatures are between T_c of 295 K and T_h of 440 K. The adiabatic oscillation is probably established in the tube section of a relatively large diameter, but the oscillation in the narrow channel of the stack is close to the isothermal oscillation.

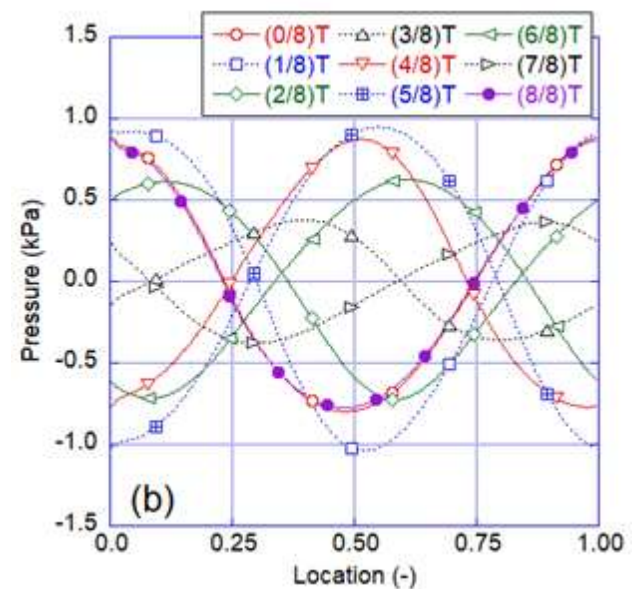
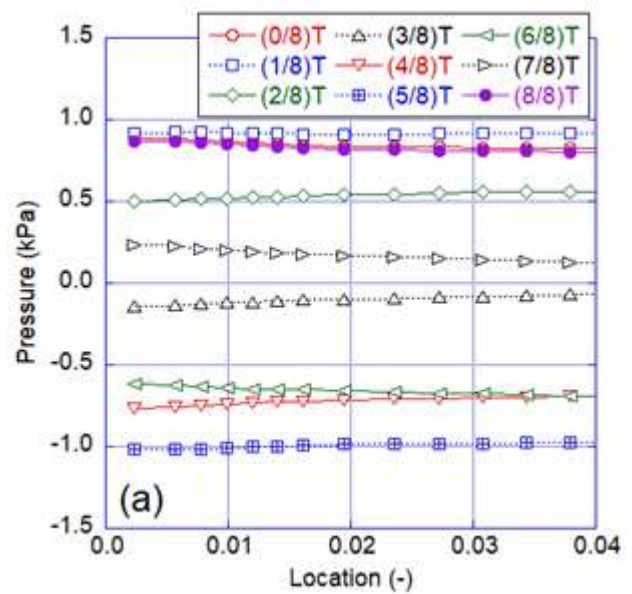


Fig. 5: Distributions of oscillating pressure during one oscillation period along the stack and the tube inlet (a) and along the loop including the stack (b).

The thermal boundary-layer thickness, $\delta_\alpha = (2\alpha/\omega)^{1/2}$, where α and ω are, respectively, the thermal diffusivity and the angular frequency, is estimated to be 0.284 mm for the average temperature in the stack, and sufficiently large compared to the channel radius of 0.4 mm. Furthermore, the thermal relaxation time, $\tau = r^2/(2\alpha)$, where r is the radius of the narrow channel, is about 2.51 ms, and sufficiently large compared to the oscillation period of 7.95 ms. The heat transfer similar to the isothermal process is, thus, expected in the stack. It is noted in Figure 4(b) that the average wave speed is in between the adiabatic sound speed of 344.5 m/s for T_c and the isothermal

sound speed of 355.2 m/s for T_h . It is found that thermoacoustic oscillation could be possible in the loop when the isothermal sound speed for the highest temperature exceeds the adiabatic sound speed for the lowest temperature. This is one of the necessary conditions for the temperature difference between the hot and cold HXs.

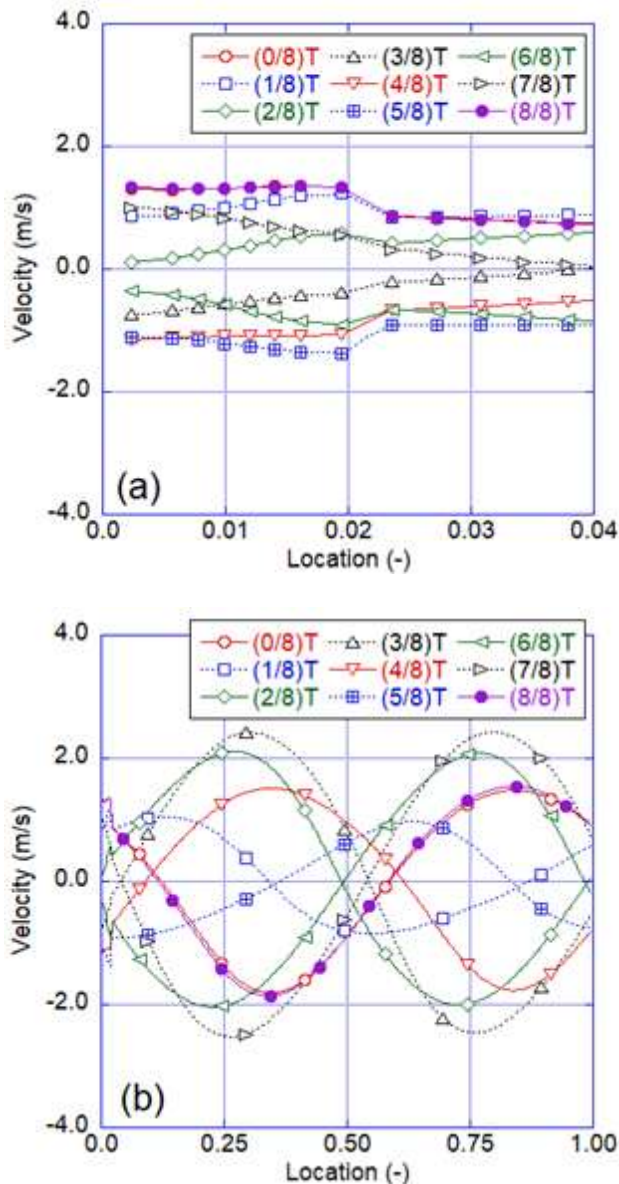


Fig. 6: Distributions of oscillating velocity during one oscillation period along the stack and the tube inlet (a) and along the loop including the stack (b).

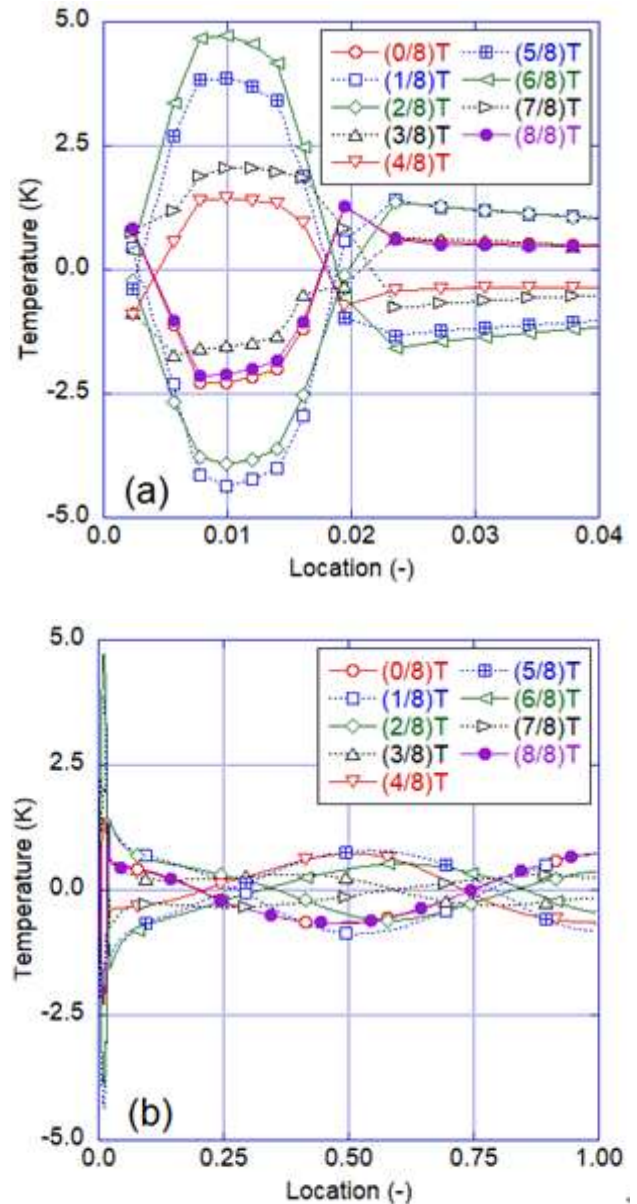


Fig. 7: Distributions of oscillating temperature during one oscillation period along the stack and the tube inlet (a) and along the loop including the stack (b).

3.4 Spatial Distribution of Oscillating Variables

The spatial distributions of oscillating pressure, velocity, and temperature along the loop are shown in Figure 5, Figure 6, and Figure 7, respectively. They are calculated as variations from their time averages. The oscillation period, T , is divided by eight, and nine distributions are shown every 0.99 ms after 5020 s in Figure 5, Figure 6, and Figure 7. The timings are denoted by $(n/8)T$, where n is from 0 to 8. It is noted that the last timing, $(8/8)T$, is 7.92 ms, and slightly shifted from the first timing, $(0/8)T$, since the oscillation period is 7.95 ms. The distributions along the stack and tube inlet are

enlarged in Figs. 5(a), 6(a), and 7(a), while those along the loop including the stack are in Figs. 5(b), 6(b) and 7(b).

The wavelength of pressure oscillation is shown to be the same as the loop length in Figure 5(b) since the loop is closed and the traveling wave is induced. The amplitude is larger at the location of the stack and $(2/4)L$ and smaller at $(1/4)L$ and $(3/4)L$. The pressure distributions in the stack, which is from the location of 0.0046 to 0.017, are almost flat in Figure 5(a). It is thus found that the pressure is oscillating continuously along the stack and the tube as a single wave.

The amplitude of velocity oscillation in Figure 6(b) is smaller at the location of the stack and $(2/4)L$ and larger at $(1/4)L$ and $(3/4)L$. The velocity distributions in the stack in Figure 6(a) are almost flat, as is the case with the pressure distributions shown in Figure 5(a), though the phase difference between the pressure and the velocity is 27.17 deg. The flow area of the stack and HXs are smaller than that of the tube, and the slight change in velocity is seen at the tube inlet, which is at about the location of 0.022 in Figure 6(a). The velocity is thus shown to be oscillating continuously along the stack and the tube as a single wave according to the flow area.

The amplitude of temperature oscillation in Figure 7(b) is larger at the location of the stack and $(2/4)L$ and smaller at $(1/4)L$ and $(3/4)L$. The oscillation timings and the spatial distributions of the temperature along the tube are similar to those of the pressure in Figure 5(b).

The temperature distributions in the stack in Figure 7(a) are, however, much different from the pressure distributions in Figure 5(a). The temperature distributions are not flat and the sign of the temperature variation is opposite to that in the tube section.

The pressure and the velocity distributions are similar in the stack as shown in Figs. 5(a) and 6(a). The gas is moving in the direction from the cold to hot HXs during the positive velocity period shown in Figure 6(a), and the temperature becomes lower due to the cold inflow as shown in Figure 7(a). When the velocity is negative, on the contrary, the gas is moving in the direction from the hot to cold HXs, and the temperature becomes higher due to the hot reverse flow. The gas is, thus, cooled and heated during the high and low-pressure periods, respectively. The sign of the temperature variation is, thus, opposite to those of the pressure and velocity variations. Both ends of the stack are open in the loop and seem to play the role of the node for temperature oscillation as seen in Figure 7(a). It is found in the stack that the temperature is oscillating

differently and the distribution of oscillating temperature is reversed from that in the tube.

3.5 Onset Temperature Ratio

The onset temperature ratio, T_h/T_c , is shown in Figure 8 as a function of the oscillation parameter $\omega\tau$. The simulation results with the constant heat transfer coefficient, [37], and the analytical results and experimental data, [31], are shown along with the present results. It is shown by the present calculations and the existing analytical and experimental results that the minimum temperature ratio of about 1.5 is obtained at around $\omega\tau$ of 2.0. This point corresponds to the calculated results shown in Figure 3, Figure 4, Figure 5, Figure 6, and Figure 7. It is seen in Figure 8 that the minimum temperature ratio for the onset of oscillation is calculated well by the present numerical procedure.

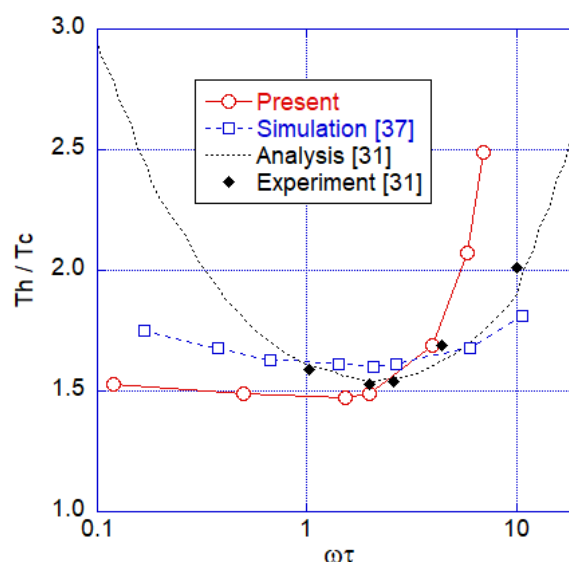


Fig. 8: Onset temperature ratio as a function of oscillation parameter.

The present results increase as $\omega\tau$ increases from the minimum point and are larger than the other results. As $\omega\tau$ decreases, the present results increase slightly, but smaller than the other results.

The heat transfer area in the stack is proportional to the product of the perimeter and the number of channels. The perimeter and the number of channels are, respectively, proportional to r and $1/r^2$. The heat transfer area is, thus, proportional to $1/r$. The heat transfer coefficient is proportional to $1/r$, since it is given by the Nusselt number, Eq. (8), which is the constant for laminar flows. The heat transfer between the gas and the wall is proportional to the product of the heat transfer area and the heat transfer coefficient, and thus to $1/r^2$ or $1/(\omega\tau)$. It is shown in Figure 8 for larger $\omega\tau$ that the heat transfer

becomes small and the onset temperature ratio is larger than the analytical and experimental results. On the contrary for smaller $\omega\tau$, the heat transfer becomes large and the onset temperature ratio is smaller than the analytical and experimental results.

The simulation results with the constant heat transfer coefficient, [37], seem to be better for larger $\omega\tau$. The Nusselt number used in this study is obtained analytically for the steady-state non-oscillating laminar flow and might be different from that for the oscillating flow. Furthermore, the distribution of oscillating temperature in the stack is reversed at a short distance from that in the tube as shown in Figure 7(a). It should also be noted that the adiabatic oscillation is established in the tube section, but the oscillation in the narrow channel of the stack is close to the isothermal oscillation.

For the practical application and design of thermoacoustic devices, the heat transfer coefficient or the heat transfer model should include above mentioned characteristics of thermoacoustic oscillation. Although the threshold of oscillation is simulated well in this study, detailed theoretical and numerical analyses and experiments would be necessary to estimate correctly the heat transfer for the oscillating flow in the narrow channel.

4 Conclusion

The thermoacoustic oscillation in the closed loop has been numerically simulated by solving the compressible mass, momentum, and energy conservation equations for the gas and the heat conduction equations for the wall. The loop was composed of the cold heat exchanger, the narrow channel section, the hot heat exchanger, and the tube. The onset of oscillation was calculated by gradually increasing the temperature of a hot heat exchanger. The minimum onset temperature ratio was shown to agree with the existing analytical and experimental results. The average wave speed was in between the isothermal sound speed for the highest temperature and the adiabatic sound speed for the lowest temperature. The distribution of oscillating temperature in the narrow channel was shown to be different and reversed from that in the tube. Although the threshold of oscillation was simulated, it was shown that the heat transfer in the narrow channel is smaller for larger channel diameter and larger for smaller channel diameter, and the heat transfer coefficient or the heat transfer model should be improved for the oscillating flow in the narrow channel.

In this study, several characteristic features of thermoacoustic oscillation, especially the spatial distribution of oscillating variables in the narrow channel, were confirmed using the fluid equations and heat conduction equations. It was shown that the safety analysis code for nuclear reactors could be used for the simulation of thermoacoustic oscillation. Applications for various configurations and conditions in nuclear engineering fields would be evaluated in the same manner, since different boundaries and initial conditions are set easily. A similar closed-loop experiment is underway by the author's group based on the present simulations for studying the applicability in the nuclear engineering fields, and experimental results would be shown in the near future.

References

- [1] Lord Rayleigh, The explanation of certain acoustical phenomena, *Nature (July 18)*, 1878, pp. 319-321.
- [2] Yazaki, T., Iwata, A., Maekawa, T., and Tominaga, A., Traveling wave thermoacoustic engine in a looped tube, *Phys. Rev. Lett.*, 81(15), 1998, pp. 3128-3131.
- [3] Feldman, K. T., Review of the literature on Sondhauss thermoacoustic phenomena, *J. Sound and Vib.* 7(1), 1968, pp. 71-82.
- [4] Feldman, K. T., Review of the literature on Rijke thermoacoustic phenomena, *J. Sound and Vib.*, 7(1), 1968, pp. 83-89.
- [5] Bisio, G., and Rubatto, G., Sondhauss and Rijke oscillations – thermodynamic analysis, possible applications and analogies, *Energy* 24,1999, pp. 117-131.
- [6] Swift, G. W., Thermoacoustic engines and refrigerators: a short course, 1999, LA-UR-99.
- [7] Yu, Z. B., Li, Q., Chen X, Guo, F. Z., and Xie, X. J., Experimental investigation on a thermoacoustic engine having a looped tube and resonator, *Cryogenics* 45, 2005, pp. 566-571.
- [8] Blok, K., Low operating temperature integral thermo acoustic devices for solar cooling and waste heat recovery, *J. Acoust. Soc. Am.* 123, 2008, 3541.
- [9] Hasegawa, S., Kondo, K., and Oshinoya, Y., Experimental verification of heat transport by acoustic wave, *Appl. Thermal Eng.* 78, 2015, pp. 551-555.
- [10] Jin, T., Yang, R., Liu, Y., and Tang, K., Thermodynamic characteristics during the onset and damping processes in a looped

- thermoacoustic prime mover, *Appl. Thermal Eng.*, 100, 2016, pp. 1169-1172.
- [11] Jin, T., Yang, R., Wang, Y., Liu, Y., and Feng, Y., Phase adjustment analysis and performance of a looped thermoacoustic prime mover with compliance/resistance tube, *Appl. Energy* 183, 2016, pp. 290-298.
- [12] Chen, G., Tang, T., and Mace, B. R., Theoretical and experimental investigation of the dynamic behavior of a standing-wave thermoacoustic engine with various boundary conditions, *Int. J. Heat Mass Trans.* 123, 2018, pp. 367-381.
- [13] Chen, G., Tang, L., and Mace, B. R., Modelling and analysis of a thermalacoustic-piezoelectric energy harvester, *Appl. Thermal Eng.* 150, 2019, pp. 532-544.
- [14] Ward, W. C., and Swift, G. W., Design environment for low-amplitude thermoacoustic engines, *J. Acoust. Soc. Am.* 95, 1994, 3671.
- [15] Piccolo, A., Numerical computation for parallel plate thermoacoustic heat exchangers in standing wave oscillatory flow, *Int. J. Heat Mass Trans.* 54, 2011, pp. 4518-4530.
- [16] Zhang, X., and Chang, J., Onset and steady-operation features of low temperature differential multi-stage travelling wave thermoacoustic engines for low grade energy utilization, *Energy Conv. Management* 105, 2015, pp. 810-816.
- [17] Kalra, S., Desai, K. P., Naik, H. B., and Atrey, M. D., Theoretical study on standing wave thermoacoustic engine, *Phys. Procedia* 67, 2015, pp. 456-461.
- [18] Wang, K., Sun, D. M., Zhang, J., Zou, J., Wu, K., Qiu, L. M., and Huang, Z. Y., Numerical simulation on onset characteristics of traveling-wave thermoacoustic engines based on a time-domain network model, *Int. J. Thermal Sci.* 94, 2015, pp. 61-71.
- [19] Napolitano, M., Dragonetti, R., and Romano, R., A method to optimize the regenerator parameters of a thermoacoustic engine, *Energy Procedia* 126, 2017, pp. 525-532.
- [20] Kruse, A., Ruziewicz, A., Nems, A., and Tajmar, M., Numerical analysis of competing methods for acoustic field adjustment in a looped-tube thermoacoustic engine with a single stage, *Energy Conv. Management* 181, 2019, pp. 26-35.
- [21] Saechan, P., and Jaworski, A. J., Numerical studies of co-axial travelling-wave thermoacoustic cooler powered by standing-wave thermoacoustic engine, *Renewable Energy* 139, 2019, pp. 600-610.
- [22] Jin, T., Huang, J., Feng, Y., Yang, R., Tang, K., and Radebaugh, R., Thermoacoustic prime movers and refrigerators: Thermally powered engines without moving components,” *Energy* 93, 2015, pp. 828-853.
- [23] Timmer, M. A. G., Blok, K., and van der Meer, T. H., Review on the conversion of thermoacoustic power into electricity, *J. Acoust. Soc. Am.* 143(2), 2018, pp. 841-857.
- [24] Normah, M. G., Irfan, A. R., Koh, K. S., Manet, A., and Zaki, Ab. M., Investigation of a portable standing wave thermoacoustic heat engine, *Procedia Eng.* 56, 2013, pp. 829-834.
- [25] Abdoulla-Latiwish, K. O. A., and Jaworski, A. J., Two-stage travelling-wave thermoacoustic electricity generator for rural areas of developing countries, *Appl. Acoust.* 151, 2019, pp. 87-98.
- [26] Yang, T., Wang, Y., Jin, T., Feng, Y., and Tang, K., Development of a three-stage looped thermoacoustic electric generator capable of utilizing heat source below 120 C, *Energy Conv. Management* 155, 2018, pp. 161-168.
- [27] Steiner, T. W., Hoy, M., Antonelli, K. B., Malekian, M., Archibald, G. D. S., Kanemaru, T., Aitchison, W., Chardon, B., Gottfried, K. T., Elferink, M., Henthorne, T., O'Rourke, B., and Kostka, P., High-efficiency natural gas fired 1 kWe thermoacoustic engine, *Appl. Thermal Eng.* 199, 2021, 117548.
- [28] Hrisko, J., and Garrett, S. L., The vibroacoustical environment in two nuclear reactors, *J. Acoust. Soc. Am.* 137, 2015, 2198.
- [29] Garrett, S. L., Smith, J. A., Smith, R. W. M., Hendrich, B. J., and Heibel, M. D., Fission-powered in-core thermoacoustic sensor, *Appl. Phys. Lett.* 108, 2016, 144102.
- [30] Rott, N., Damped and thermally driven acoustic oscillations in wide and narrow tubes, *Z. Angew. Math. Phys.* 20, 1969, pp. 230-243.
- [31] Ueda, Y., and Kato, C., Stability analysis of thermally induced spontaneous gas oscillations in straight and looped tubes, *J. Acoust. Soc. Am.* 124, 2008, pp. 851-858.
- [32] Nowak, I., Rulik, S., Wroblewski, W., Nowak, G., and Szwedowicz, J., Analytical and numerical approach in the simple modelling of thermoacoustic engines, *Int. J. Heat Mass Trans.* 77, 2014, pp. 369-376.
- [33] Rogozinski, K., Nowak, I., and Nowak, G., Modeling the operation of a thermoacoustic engine, *Energy* 138, 2017, pp. 249-256.

- [34] Skaria, M., Rasheed, K. K. A., Shafi, K. A., Kasthuriengan, S., and Behera, U., Simulation studies on the performance of thermoacoustic prime movers and refrigerator, *Comp. Fluids* 111, 2015, pp. 127-136.
- [35] Sun, D., Wang, K., Guo, Y., Zhang, J., Xu, Y., Zou, J., and Zhang, X., CFD study on Taconis thermoacoustic oscillation with cryogenic hydrogen as working gas, *Cryogenics* 75, 2016, pp. 38-46.
- [36] Hussain, M. N., and Janajreh, I., Analysis of pressure wave development in a thermoacoustic engine and sensitivity study, *Energy Procedia* 142, 2017, pp. 1488-1495.
- [37] Watanabe, T., Numerical simulation of thermo-acoustic gas oscillation for nuclear application, *Int. J. Multiphysics* 16, 2022, pp. 1-13.
- [38] RELAP5-3D Code Development Team, RELAP5-3D Code Manual, 2015, INL/MIS-15-36723.

Contribution of Individual Authors to the Creation of a Scientific Article (Ghostwriting Policy)

Tadashi Watanabe has performed all the research works in this study; planning, literature survey, numerical simulation, discussion, writing, and so on.

Sources of Funding for Research Presented in a Scientific Article or Scientific Article Itself

No funding was received for conducting this study.

Conflict of Interest

The authors have no conflict of interest to declare.

Creative Commons Attribution License 4.0 (Attribution 4.0 International, CC BY 4.0)

This article is published under the terms of the Creative Commons Attribution License 4.0

https://creativecommons.org/licenses/by/4.0/deed.en_US